Journal of Membrane Science 437 (2013) 196–204

Contents lists available at SciVerse ScienceDirect

Journal of Membrane Science

journal homepage: www.elsevier.com/locate/memsci

Modeling of hydrogen permeation for Ni–BZCY asymmetric membrane

Qingping Zhang [a], Zhiwen Zhu [a], Tong Liu [a], Wei Liu [a,b,*]

[a] CAS Key Laboratory of Materials for Energy Conversion, Department of Material Science and Engineering, University of Science and Technology of China, Hefei 230026, PR China
[b] Key Laboratory of Materials Physics, Institute of Solid State Physics, Chinese Academy of Sciences, Hefei 230031, China

ARTICLE INFO

Article history:
Received 8 January 2013
Received in revised form
3 March 2013
Accepted 7 March 2013
Available online 16 March 2013

Keywords:
Hydrogen permeation
Model
Asymmetric structure
Cermet membrane

ABSTRACT

Hydrogen separation membrane of Ni–$BaCe_{0.7}Zr_{0.1}Y_{0.2}O_{3-\delta}$ cermet with an asymmetric structure was simulated by considering several involved processes, such as mass transportation in porous support, bulk diffusion in dense layer, interfacial exchange on both sides of the membrane, and hydrogen permeation through nickel phase. The model was compared with experimental results and could match them in general. Equivalent resistances of each step in asymmetric membrane were introduced to determine their influence on the performance and recognize the rate-determining step. Advice on further capacity improvement was given based on the simulation results. This model could be used to analyze and predict the performance of this kind of asymmetric hydrogen separation membrane.

1. Introduction

Hydrogen separation membranes have received considerable attention these years for their potential employments in hydrogen based industry, such as dehydrogenation reactions that require selective removal of hydrogen, water-gas shift reactions [1], and methane reforming [2,3] to produce pure hydrogen. A ceramic hydrogen separation membrane is known for its lower cost than the Pd alloy membrane and high selectivity, and thus has aroused great interests.

Various kinds of ceramic proton conductors have been discovered since the pioneer work of Iwahara et al. [4], such as doped perovskite ($BaCeO_3$, $SrCeO_3$, $BaZrO_3$, etc.), doped $La_2Zr_2O_7$ [5], $Ba_3Ca_{1.18}Nb_{1.82}O_{9-\delta}$ (BCN18) [6,7], $La_2Ce_2O_7$ [8], $La_{28}W_4O_{54}$ [9] and so on. Doped $SrCeO_3$, a stable proton–electron mixed conductor, has already been applied to hydrogen permeation [10]. Among these materials, proton conductivity of doped $BaCeO_3$ is the highest. Zr–Y doped $BaCeO_3$ (BZCY) is a good candidate of proton conductor because of its balance between conductivity and stability [11,12]. However, considering its low electronic conductivity [13] under reducing atmosphere, a metal phase (usually nickel) is composed to form a cermet composite.

Two configurations, namely symmetric and asymmetric structures, can be adopted for gas separation membranes. Asymmetric gas separation membrane has great advantages over symmetric one. As the thickness of dense layer becomes thinner, bulk diffusion resistance will be dropped accordingly. Thus, a higher permeation rate than that of symmetric membrane is expected. For instance, Tosti et al. have reported a hydrogen selective membrane with Pd–Ag alloy thin layer and stainless steel grids substrate, aiming at cost reduction and performance enhancement [14]. Zhu et al. have already successfully fabricated Ni–BZCY asymmetric membrane with high permeation rate [15]. However, the structure of at least two layers makes the fabrication of asymmetric membrane more complicated.

As to the simulation of asymmetric structure, several models have been reported. For example, Beuscher et al. have put forward their asymmetric model for the selective permeation of trichloroethylene vapor mixed with nitrogen. By considering the effects of boundary layers at membrane surface, bulk diffusion in dense membrane and gas transportation within support, an accurate description of experimental data could be achieved [16,17]. Caravellaa et al. have studied hydrogen permeation in Pd-alloy based asymmetric membrane [18]. In their improved model, not only the phenomena mentioned above, but also hydrogen adsorption and dissociation on the palladium surface were taken into account. Chang et al. have discussed the modes of oxygen permeation for asymmetric mixed-conductor membrane [19]. Two ways of oxygen transport within support were distinguished separately, namely transport through support only by molecule diffusion in the pores, and through walls within a depth of the support (see Fig. 3 of that reference).

For the Ni–BZCY composite asymmetric hydrogen permeation membrane, there are some characteristics which are distinct from others above. As dual phase is applied, the effective properties of each phase are quite different from the bulk ones in view of the percolation theory. Besides, unlike those asymmetric structure of

* Corresponding author at: CAS Key Laboratory of Materials for Energy Conversion, Department of Material Science and Engineering, University of Science and Technology of China, Hefei 230026, PR China. Tel.: +86 551 6360 6929; fax: +86 551 3601 592.
E-mail address: wliu@ustc.edu.cn (W. Liu).

0376-7388/$ - see front matter © 2013 Elsevier B.V. All rights reserved.
http://dx.doi.org/10.1016/j.memsci.2013.03.010

single phase, interfacial exchange at three phase boundary (TPB), where ionic phase, electronic phase and gaseous phase joint together, is special in Ni–BZCY cermet. In addition, since nickel can also permeate hydrogen, contribution from Ni path to the total hydrogen permeation needs to be taken account of.

Unlike symmetric structure without support of the previous work [20], the support of asymmetric membrane can influence the permeation in two ways. First, porous support would cause a concentration polarization, leading to a decrease of hydrogen partial pressure at membrane-support interface (MSI) compared with that outside the membrane. Second, interfacial exchange could take place both at MSI and extended into the porous support within several particle layers, which is unique in the asymmetric membrane. The introduction of asymmetric structure can reduce the thickness of the dense membrane, and provide enlarged active zone at porous side, both of which are helpful to the enhancement of the hydrogen permeation.

In this paper, a mathematical model for Ni–$BaCe_{0.7}Zr_{0.1}Y_{0.2}O_{3-\delta}$ cermet hydrogen separation membrane with an asymmetric structure is proposed and then compared with the experiment. In this model most involved phenomena are included, such as gas transportation in porous support, bulk diffusion in dense layer, surface exchange at both sides of the membrane, and the permeation from Ni phase. Interfacial polarization within support and at MSI is considered separately in an explicit way. Analyses of the contributions from participated phenomena in hydrogen permeation could give an insight into the asymmetric membrane, and are helpful to the prediction and improvement of the membrane performance.

2. Model description

Disk-shaped asymmetric samples are simulated in this model. Just the same as experimental settings, volume fractions of BZCY phase in substrate and dense membrane are 0.7 and 0.6 respectively. Porous support is located at hydrogen rich side.

As to the surface exchange, two steps are considered when protons are incorporated into the BZCY lattice near the TPB

$$H_2 + 2* \Leftrightarrow 2H_* \quad \text{(stepI)}$$

$$H_* + O_O^{\times} \Leftrightarrow OH_O^{\bullet} + * + e^- \quad \text{(stepII)}$$

where H_* and $*$ are sites adsorbed by hydrogen atom and vacant sites at Ni surface respectively.

The former step is the adsorption or dissociation of hydrogen molecule on nickel surface at hydrogen rich (HR) or hydrogen lean (HL) side; and the latter one stands for the incorporation of adsorbed atom into the lattice oxygen of BZCY at HR side, and its inverse process at HL side.

According to the previous model for symmetric membrane [20], step I is quasi-equilibrium under the experimental conditions, and step II is the rate limiting step of surface exchange. The reaction rate of step II at unit TPB area could be expressed as

$$r_{2,MSI} = k_1\,\theta_{MSI} - k_2\,C_{MSI}(1-\theta_{MSI}) \text{ at HR side} \tag{1a}$$

$$r_{2,L} = k_2\,C_L(1-\theta_L) - k_1\theta_L \text{ at HL side} \tag{1b}$$

where k_1 and k_2 are rate constants of the forward and backward reactions of step II; C_{MSI} and C_L are the $OH_O^{\bullet}$ $OH_O^{\bullet}$ concentration of the surface BZCY particles at MSI and HL side respectively; θ_{MSI} and θ_L are the hydrogen atom coverage at Ni surface of related sides.

For quasi-equilibrium step I, equilibrium constant K is defined as

$$K = \frac{\theta_H^2}{p_{H_2}(1-\theta_H)^2} \tag{2}$$

where θ_H is hydrogen atom coverage, and p_{H_2} is hydrogen partial pressure. The parameters needed to calculate K could be found in Ref. [21].

In this model, several approximations are made for simplification. First, surface kinetics of step I above is not considered as rate limiting step. Considering that Ni is a good catalyst for hydrogen adsorption and dissociation, the influence of this process is relatively smaller than step II that BZCY involved in. Second, all particles are viewed as spheres with the same radius, since BZCY and Ni particles are similar in shape and size for the tested samples in SEM images. Third, concentration boundary layers at membrane surfaces are ignored for the relatively low permeation rate. Fourth, the radial distribution of each species in disk-shaped asymmetric sample is neglected, which is rational because of much smaller size along the axial direction than the radial one.

2.1. Concentration polarization within the support

So far, several mass transfer models to predict the concentration polarization in porous substrate are developed, such as the Stefan–Maxwell model (SMM), the dusty gas model (DGM), and Binary Friction Model (BFM) [22]. Ref. [23] compared these models above in the application of SOFC anode. They have argued that the prediction of DGM is similar to that of BFM in studied cases, but the former one is of much less computational cost. While for the SMM model, since the absence of description to the Knudsen diffusion phenomenon in substrate with small pores, the results could be less accurate. Therefore, DGM, which includes interaction among molecules, Knudsen diffusion and viscous flow of porous media, is adopted in this model. The equation of DGM is given by [24]

$$\sum_{l\neq k}\frac{x_l N_k - x_k N_l}{x_T D_{kl}^{eff}} + \frac{N_k}{D_{k,Kn}^{eff}} = -\nabla x_k - \frac{x_k}{D_{k,Kn}^{eff}}\frac{B}{\mu_m}\nabla p \tag{3}$$

where x_k is the molar concentration of gaseous species k; x_T is the total molar concentration; N_k is the net molar flux of species k; $D_{k,Kn}^{eff}$ and D_{kl}^{eff} are the effective Knudsen diffusion coefficient and binary diffusion coefficient of related gaseous species; B is the dimensional permeability constant, and μ_m is the dynamic viscosity of gas mixture. DGM model is simplified to one dimension along axial direction for the assumption that all species are evenly distributed along radial direction as mentioned above.

In this situation, gaseous species are H_2 and N_2 at HR side. Under steady state, N_{H_2} is equal to the consumption rate of hydrogen. N_{N_2} should be zero because nitrogen is inert species not consumed in interfacial exchange [24]. Geometric parameters for porous support in this model are kept identical to the tested samples, with substrate porosity $\phi_g = 0.4$, pore radius $r_g = 0.3$ μm, and support thickness $L = 1.5$ mm. Parameters and formulae needed to calculate $D_{k,Kn}^{eff}$ and D_{kl}^{eff} are taken from Ref. [26]. The tortuosity of the support (τ_g), which is used to figure out $D_{k,Kn}^{eff}$ and D_{kl}^{eff}, is set to 5 in common [25,27]. Dynamic viscosity μ_m can be obtained by Wilke's method from the viscosities of pure components [28]. The permeability constant B is determined by Carman–Kozeny correlation [29]. Since no analytic solution can be derived from Eq. (3), numerical scheme with iteration is employed, as depicted in Ref. [23–25].

2.2. Interfacial polarization at HR side

Since interfacial polarization occurs at both MSI and extended TPB area of HR side, it will be divided into two parts (denoted as J_{MSI} and J_s respectively) and discussed below.

Fig. 1 shows the diagram of reaction area extended into support and at MSI. Only part of the support within the depth of δ actually participates in the interfacial exchange; while outside this range, it becomes inactive. Typically, δ is in the magnitude of 10 μm, which

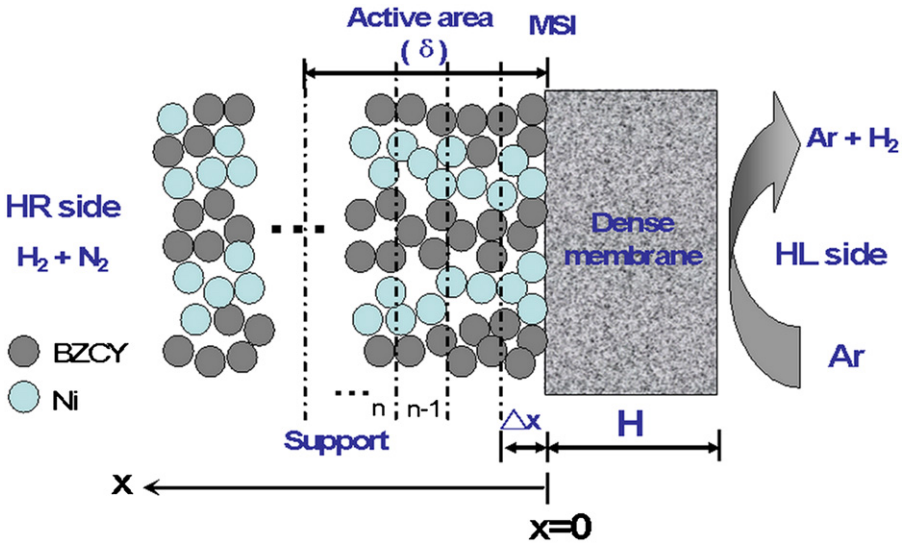

Fig. 1. Diagrammatic sketch of asymmetric structure with porous support, MSI and dense membrane.

is the thickness of several particle layers, as reported in ionic conductor [30]. Accordingly, δ is estimated as 10 μm in this model.

To determine J_{MSI}, the active area within support is divided into tiny layers with a thickness of Δx (see Fig. 1). The proton flux through the nth layer of active zone is

$$J_n = D_s^{eff}\frac{c_{n+1}-c_n}{\Delta x} \tag{4}$$

where C_n is the OH_O^* concentration of the nth layer; and D_s^{eff} is the effective diffusion coefficient of OH_O^* in the support, and could be estimated from bulk diffusion coefficient (D_0) of BZCY using the percolation theory [20]. D_0 could be derived from experimental data of symmetric membrane following the procedure in Ref. [20], and is fitted as $D_0 = 8.4\times10^{-7}\exp(-7820/T)$ under reducing atmosphere.

The reaction rate at unit TPB area of nth layer is

$$r_n = k_1\theta_n - k_2 c_n(1-\theta_n) \tag{5}$$

where θ_n is the coverage of hydrogen atom at Ni surface in nth layer. Although θ_n is dependent with p_{H_2}, which is different at each tiny layer; it should be noticed that extended TPB area is only limited in the vicinity of MSI (around 10 μm). Thus p_{H_2} within this range could be approximated to the hydrogen partial pressure at MSI (p_{MSI}). Besides, as shown in section 3.3.1, concentration polarization is not noticeable for Ni–BZCY asymmetric membrane, resulting in only a small change of p_{H_2} through the support. Hence, θ_n is approximated to θ_{MSI} and independent with the location.

According to the mass conservation of nth layer

$$J_{n-1}S = r_n w L_s S\Delta x + J_n S \tag{6}$$

where w is TPB width, L_s is TPB length of the support in unit volume, and S is the cross section of the membrane.

Substituting J_{n-1}, J_n and r_n into Eq. (6) and letting $\Delta x\to 0$, a differential equation of two order is obtained

$$-D_s\frac{d^2c(x)}{dx^2} = L_s w\left[k_1\theta_{MSI} - k_2(1-\theta_{MSI})c(x)\right] \tag{7}$$

with boundary conditions given as

$$\frac{dc(x)}{dx}|_{x=\delta} = 0 \tag{8a}$$

and

$$c(x=0) = c_{MSI} \tag{8b}$$

The analytic solution of Eq. (7) is

$$c(x) = c_{eq} - (c_{eq}-c_{MSI})\frac{\cos h(\frac{\delta}{\tau}-\frac{x}{\tau})}{\cos h(\frac{\delta}{\tau})} \tag{9}$$

where

$$c_{eq} = \frac{k_1\theta_{MSI}}{k_2(1-\theta_{MSI})} \tag{9a}$$

and

$$\tau = \sqrt{\frac{D_s}{k_2 w L_s(1-\theta_{MSI})}}. \tag{9b}$$

The contribution of proton flux from support is thus given as

$$J_s = \left|-D_s\frac{dc}{dx}(x=0)\right| = D_s\frac{c_{eq}-c_{MSI}}{\tau}\tan h(\frac{\delta}{\tau}) \tag{10}$$

Another part, J_{MSI}, can be expressed as

$$J_{MSI} = [k_1\theta_{MSI} - k_2 c_{MSI}(1-\theta_{MSI})]L_m\phi_g w \tag{11}$$

where L_m is TPB length on the dense membrane surface in unit area. In Eq. (11), ϕ_g is multiplied because at MSI only the area exposed to gaseous phase is active for interfacial exchange.

2.3. Determination of hydrogen permeation rate

Two paths are available for hydrogen permeation, either through BZCY or Ni. Both of them are considered in this model. For BZCY phase, the proton flux, J_{io}, is decided as follows.

$$J_{io} = J_s + J_{MSI} \text{ at HR side} \tag{12}$$

$$J_{io} = [k_2 c_L(1-\theta_L) - k_1\theta_L]L_m w \text{ at HL side} \tag{13}$$

If the effect of concentration boundary layer is neglected

$$J_{io} = D_m\frac{c_{MSI}-c_L}{H} \tag{14}$$

where D_m is the effective diffusion coefficient of dense membrane, which is also estimated from D_0 by the percolation theory; and H is the thickness of dense membrane.

Combining Eqs. (2, 9a, 10–14), the solution of J_{io} is

$$J_{io} = \frac{\frac{k_1}{k_2}\sqrt{K}(\sqrt{p_{MSI}}-\sqrt{p_L})}{\frac{H}{D_m}+\frac{1}{P+Q}+\frac{1}{N}} \tag{15}$$

Where $P=\frac{D_s}{\tau}\tan h(\frac{\delta}{\tau})$, $Q=k_2w(1-\theta_{MSI})L_m\phi_g$, $N=k_2w(1-\theta_L)L_m$; p_{MSI} and p_L are hydrogen partial pressure at MSI and lean side, respectively. Since $k_1'=k_1w$ and $k_2'=k_2w$ are given in Ref. [20], the related parameters above are rewritten accordingly. The representation for asymmetric structure is similar to that of symmetric one [20], except the terms (P and Q) at HR side. This reflects the structural difference between symmetric and asymmetric membranes.

The contribution of Ni is described by Sielverts' law, with a modification by percolation theory for the tortuosity of path in Ni–BZCY composite

$$J_{\mathrm{Ni}}=\frac{\Phi}{H}(\sqrt{p_{MSI}}-\sqrt{p_L})(\phi_{el}P_{el})^{\mu}\phi_g \tag{16}$$

where ϕ_{el} is the volume fraction of Ni in solid composite; P_{el} is the percolation probability of Ni phase calculated by the percolation theory [31]; μ is Braggeman factor [31]; and $\Phi=4.65\times 10^{-7}e^{-6440/T}$ (mol m^{-1} s^{-1} Pa$^{-0.5}$) [32].

The total hydrogen permeation rate is viewed as the sum of contributions from BZCY and Ni

$$J_{\mathrm{H_2}}=0.5J_{io}+J_{\mathrm{Ni}} \tag{17}$$

It is mentioned that, p_L in Eq. (15) is decided by $J_{\mathrm{H_2}}$ as

$$p_L=\frac{J_{\mathrm{H_2}}S}{J_{\mathrm{H_2}}S+F}p_0 \tag{18}$$

where F is the flux of sweep gas (Ar) at HL side, which is 20 mL/min in this experiment. Finally, DGM in Section 2.1 and Eq. (17) are combined together, and iteration is performed until p_{MSI} and $J_{\mathrm{H_2}}$ are consistent with each other.

2.4. Definitions of equivalent resistances

To analyze the impact of each process to the total performance, some equivalent resistances are introduced. In this model, the driven force of hydrogen partial pressure across dense membrane is defined as $\sqrt{p_{MSI}}-\sqrt{p_L}$. Then Eq. (17) would be adapted to

$$J_{\mathrm{H_2}}=\frac{\sqrt{p_{MSI}}-\sqrt{p_L}}{R_m+R_L+\frac{R_sR_{MSI}}{R_s+R_{MSI}}}+\frac{\sqrt{p_{MSI}}-\sqrt{p_L}}{R_{\mathrm{Ni}}} \tag{19}$$

where R_m stands for the resistance from bulk diffusion in dense thin membrane; R_s, R_{MSI}, and R_L are resistances from interfacial exchange at extended TPB zone within support, MSI and HL side, respectively; and R_{Ni} is the resistance from Ni path. Their representations are

$$R_m=\frac{2H}{D_m\frac{k_1'}{k_2'}\sqrt{K}} \tag{20a}$$

$$R_s=\frac{2\tau}{D_s\tan h(\frac{\delta}{\tau})\frac{k_1'}{k_2'}\sqrt{K}} \tag{20b}$$

$$R_{MSI}=\frac{2}{k_1'(1-\theta_{MSI})L_{MSI}\phi_g\sqrt{K}} \tag{20c}$$

$$R_L=\frac{2}{k_1'(1-\theta_L)L_m\sqrt{K}} \tag{20d}$$

$$R_{\mathrm{Ni}}=\frac{H}{\Phi(\phi_{el}P_{el})^{\mu}\phi_g} \tag{20e}$$

The resistance of concentration polarization within support is defined similarly

$$R_t=\frac{\sqrt{p_{\mathrm{H_2}}}-\sqrt{p_{MSI}}}{J_{\mathrm{H_2}}} \tag{20f}$$

Based on Eq. (19), an equivalent circuit could be drawn. Fig. 2 illustrates the diagrammatic sketch for this kind of asymmetric membrane. R_s and R_{MSI} are connected in parallel ($R_s//R_{MSI}$, denoted as R_{HR}), representing the interfacial exchange at HR side. R_L+R_{HR} is the total interfacial polarization for BZCY path (denoted as R_{int}).

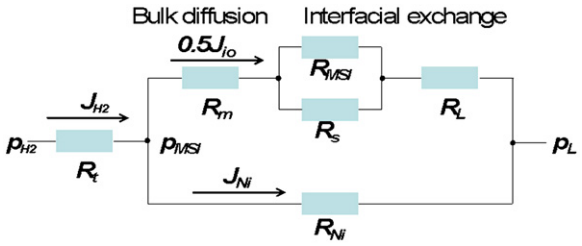

Fig. 2. Equivalent circuit of asymmetric structure.

3. Results and discussions

The results obtained by this model are compared with experimental measurements first. All experimental data are taken from our group's work, which is in preparation and will be given elsewhere [33]. The description of experimental equipment and method could be found in Ref. [15] in detail. In view of the small deviation of surface morphology and grain size between tested samples in practice, an exactly prediction is unlikely. Instead, upper and lower limits of hydrogen permeation rates are predicted using this model to give an expected range. Since particle radii of Ni–BZCY samples are mainly within the scope of 0.4–0.5 μm in SEM images, the upper, middle and lower ranges of predicted permeation rates therefore correspond to the model results with particle radii of 0.4, 0.45 and 0.5 μm respectively.

3.1. Partial pressure dependence

Samples with 27.6 μm-thick dense layer were used to reveal the dependence between $p_{\mathrm{H_2}}$ and $J_{\mathrm{H_2}}$. Hydrogen partial pressure of 0.2, 0.4, 0.6 and 0.8 atm was applied. Parameters for the asymmetric membrane model were taken the same as the tested conditions.

Both experimental data and model results of hydrogen partial pressure dependence are shown in Fig. 3. Upper and lower limits of predictions are given as error bars. The upper limits are the model results with smaller particle radius (0.4 μm), because longer TPB length on the membrane surface is available for finner grain size. The difference between upper and lower limit is around 15%, indicating a considerable influence of the grain size. Besides, shifts of measured results from the upper limit (finer grain size) to the lower limit (coarser grain size) are found. Considering that experimental data under the same partial pressure was recorded from higher to lower temperature, this trend of shift as time going on is probably an indication of grain coarsening for thin dense membrane during permeation test. In Fig. 3, most experimental data can fall into the expected ranges, implying the model validation. In general, the hydrogen partial pressure dependence could be depicted via this model within the tested temperature range and various hydrogen partial pressure. Permeation rates increase as $p_{\mathrm{H_2}}$ grows; and the increment as temperature rises is more remarkable for higher hydrogen partial pressure than lower partial pressure.

3.2. Thickness dependence

In this part, hydrogen permeation rates of five samples with different dense membrane thicknesses were measured under fixed hydrogen partial pressure of 0.2 atm. All samples were tested under five different temperatures (i.e. 1173, 1123, 1073, 1023 and 973 K). Fig. 4 compares experimental data and expected limits

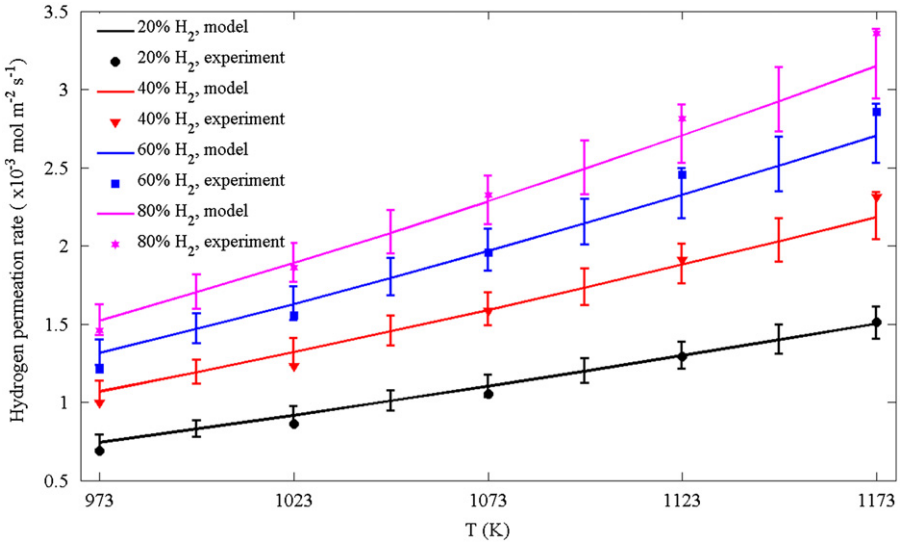

Fig. 3. Model and experimental results of sample with 27.6 μm dense layer under different hydrogen partial pressure. The upper, middle and lower ranges of error bars represent the model results with grain size of 0.4, 0.45 and 0.5 μm respectively.

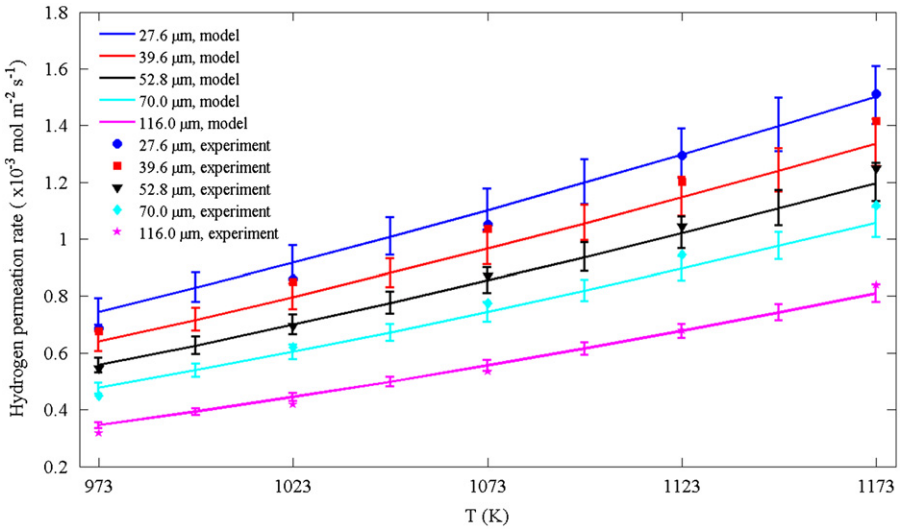

Fig. 4. Comparison of measurements and model results for samples with different thicknesses under hydrogen partial pressure of 0.2 atm. The upper, middle and lower ranges of error bars represent the model results with grain size of 0.4, 0.45 and 0.5 μm respectively.

given by this model. Again in general, most of the measured points under different thicknesses and varied temperatures could fall within the predicted ranges. It also shows that this model could be validated within a relatively broad range of tested conditions.

It appears that with the decreasing of membrane thickness, hydrogen permeation rate increases but with a slower increment. And when the membrane is relatively thin, the increment is not very obvious. For example, for the thinnest 27.6 μm and 39.6 μm samples, it is clear that with 30% reduction of dense layer thickness, permeation rate only rises no more than 15% at 1173 K as given by this model, which is disproportionate to the decreasing amplitude of membrane thickness. This is attributed to the dominating step of interfacial exchange rather than bulk diffusion in this situation. It could be deduced that a noticeable improvement of hydrogen permeation rate by reducing the membrane thickness can be achieved only when the dense membrane is relatively thick.

On the basis of the comparison between experiment and model above, a procedure of performance prediction for the Ni–BZCY asymmetric membrane via this model could be applied as follows. The particle radius distribution needs to be determined first. For a given range of grain size and tested conditions, the expected upper and lower limits can be obtained using this model. Experimental measurements are likely to stay within this predicted range. Mention that as to other similar cermet systems, modifications should be made when using this model. Some inherent properties for various cermets, such as conductivity, protonic diffusion coefficient, as well as the rate constants (k_1 and k_2) need to be refined to fit the given material. Besides, for different dual phase cermets, changes may occur in the preparation condition and sintering temperature, leading to various micro-structures and particle radii. Both of these factors cause particular parameters for different material systems used in the model. Once the parameters of these inherent properties are obtained from literature or experiment, the model has the potential to analyze and predict other similar asymmetric cermet hydrogen separation membranes.

3.3. Equivalent resistances of related processes

To identify the contribution of each process involved in asymmetric membrane separately, equivalent resistances defined above

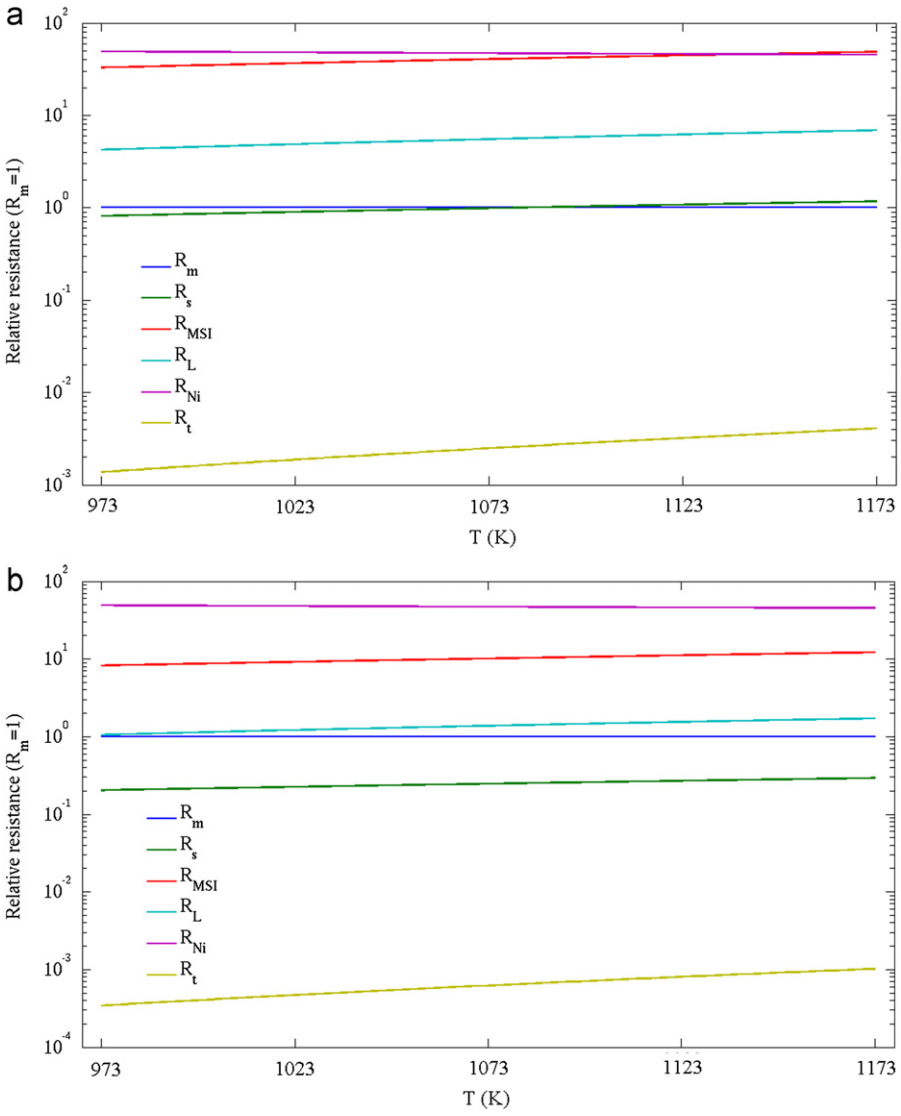

Fig. 5. Relative equivalent resistances with respect to R_m under fixed hydrogen partial pressure of 0.2 atm, with dense layer thickness of 30 μm (a), and dense layer thickness of 120 μm (b), respectively.

will be discussed. In the following section, some geometric parameters will be kept fixed, such as substrate thickness L=1.5 mm and substrate porosity ϕ_g=0.4. While the thickness of the dense layer, temperature and particle radius are variable to simulate different tested conditions. To clearly quantify the influence of each participated process under given conditions, relative quantities of each resistance with respect to R_m are applied below.

Fig. 5 illustrates the relative resistance to R_m for each process, with hydrogen partial pressure of 0.2 atm and particle radius of 0.5 μm. Two membrane thicknesses, i.e. 30 μm and 120 μm, are selected to represent relatively thinner or thicker cases, as shown in Fig. 5(a) and (b) respectively. Several magnitudes of variation among these defined resistances could be found in these figures, indicating different importance of these processes. On this basis, some useful conclusions and suggestions are made, as given below.

3.3.1. *Effect of concentration polarization*

In Fig. 5, resistances from concentration polarization within the substrate in both cases are the lowest among all resistances, about 2–3 magnitudes lower than those from bulk diffusion. Therefore, for this kind of cermet asymmetric hydrogen separation membrane, concentration polarization is less significant and thus negligible. It can be mainly ascribed to the comparably lower permeation rate (10^{-7}–10^{-8} mol cm^{-2} s^{-1}) in hydrogen separation membrane than that in SOFC (usually up to 10^{-6} mol cm^{-2} s^{-1} when peak power density is reached). Besides, the lighter molecular weight of H_2 makes the diffusivity of hydrogen in mixed gas much more faster and easier, also leading to a low concentration polarization.

3.3.2. *Interfacial exchange at HR and HL side*

At HR side, both MSI and extended TPB area can partake in the surface exchange, but they are quite distinct in proportion. In Fig. 5, R_{MSI} is about several ten times as great as R_s. Extended TPB zone within support exhibits a much lower resistance and hence is expected to be the major reaction area at HR side. On the contrary, TPB length at MSI is much less because of fewer effective connections to the gas phase and little surface area compared with extended zone, resulting in a higher resistance.

Besides, total resistance at HR side (R_{HR}, namely R_s//R_{MSI}) is much lower than that at HL side owing to the advantage of asymmetric structure. Asymmetric configuration at HR side would provide an extended TPB area deep into the substrate, and hence

more extra active reaction zone is available at this side. Because of no extended TPB zone at HL side, it implies that modification at HL side is more demanding, and has more potential to reduce the total interfacial polarization for this kind of asymmetric membrane.

One practical way to reduce interfacial exchange resistance is grain refining. Taking samples of 30 μm-thick dense layer, operated under 973 K and 20% hydrogen partial pressure, with different particle radii as example, Fig. 6 shows the calculated R_L/R_m at HL side and R_{HR}/R_m at HR side. It is evident in this figure that, with the growth of grain size, interfacial exchange becomes more significant. This can be explained by the percolation theory that, the finer the grain size, the longer the effective TPB length at membrane surface. Therefore low resistances at both sides are obtained for samples with small particle radius.

3.3.3. Comparison between bulk diffusion and interfacial exchange

In Fig. 5, resistance from bulk diffusion process (R_m) is smaller than that from interfacial polarization of HL side (R_L) for asymmetric structure with thinner dense layer (30 μm). Whereas for thicker dense layer (120 μm), they are comparable. This implies a change of dominant step from interfacial process to bulk diffusion in BZCY path as membrane thickness varies. To characterize the proportion of resistance from bulk diffusion to the total one in the BZCY path (R_m+R_{int}), w_m is defined as

$$w_m = \frac{R_m}{R_m + R_L + \frac{R_{MSI}R_s}{R_{MSI}+R_s}} \tag{21}$$

Fig. 7 shows the relationship between w_m and dense layer thickness under 973 and 1173 K, with hydrogen partial pressure of 0.2 atm and particle radius of 0.5 μm. The increase of w_m with membrane thickness indicates that bulk diffusion process is more remarkable for thicker membranes. At 973 K for example, for 30 μm sample R_m only occupies about 15% of total resistance through the BZCY path; while for 120 μm one, the ratio increases to about 45%. It is found via this model that, for the samples with dense layer thickness of less than 150 μm, interfacial exchange remains the dominant process under 973 K. Hence, the effort of enhancing permeation performance only by decreasing membrane thickness is not favored for thinner membranes, especially when dense layer is already less than 40 μm thick, because R_m only occupies a small percentage. Fig. 7 also depicts that w_m is slightly higher at a lower temperature, which could be explained by the decrease of ionic conductivity when temperature drops.

From the discussions above, it is advisable that, for thinner membranes, grain refining to increase the TPB length or surface modification at HL side is more effective to improve permeation capacity than thickness reduction, since interfacial exchange is severe for asymmetric membranes with thin dense layers.

3.3.4. Hydrogen permeation through BZCY and Ni path

Fig. 5 also illustrates that hydrogen permeation through the Ni phase is less in comparison with that through the BZCY phase because the resistance from Ni phase (R_{Ni}) is the highest one. To quantitatively analyze the contribution from these two paths, the proportion of hydrogen permeation through the BZCY path is defined as

$$w_{io} = \frac{R_{Ni}}{\frac{R_{MSI}R_s}{R_{MSI}+R_s} + R_m + R_L + R_{Ni}} \tag{22}$$

Fig. 8 shows the dependence of w_{io} on the dense membrane thickness at 973 and 1173 K, with hydrogen partial pressure of 0.2 atm and particle radius of 0.5 μm. Apparently, hydrogen permeation is mainly derived from BZCY phase. It appears that the ratio of Ni path becomes more remarkable for thinner membranes, but still nearly an order of magnitude less than that of BZCY path. Taking 973 K case as example, the proportion from Ni path is about 4% for 120 μm sample; while for 30 μm sample it increases to about 12%. It could also be found in Fig. 8 that w_{io} is a little higher at lower temperature.

4. Conclusions

A mathematical model for the Ni–BZCY cermet hydrogen separation membrane with an asymmetric structure is developed by considering the influence of concentration polarization, interfacial exchange, bulk diffusion and Ni contribution. Generally speaking, the modeling results are in agreement with the experimental data. A procedure of performance prediction using this model is given. Then equivalent circuit and resistances are introduced to probe into the corresponding processes. It turns out that concentration polarization within support is a secondary factor, while the resistance from interfacial exchange is severe especially for thin membranes. Hence, it is suggested that grain refinement

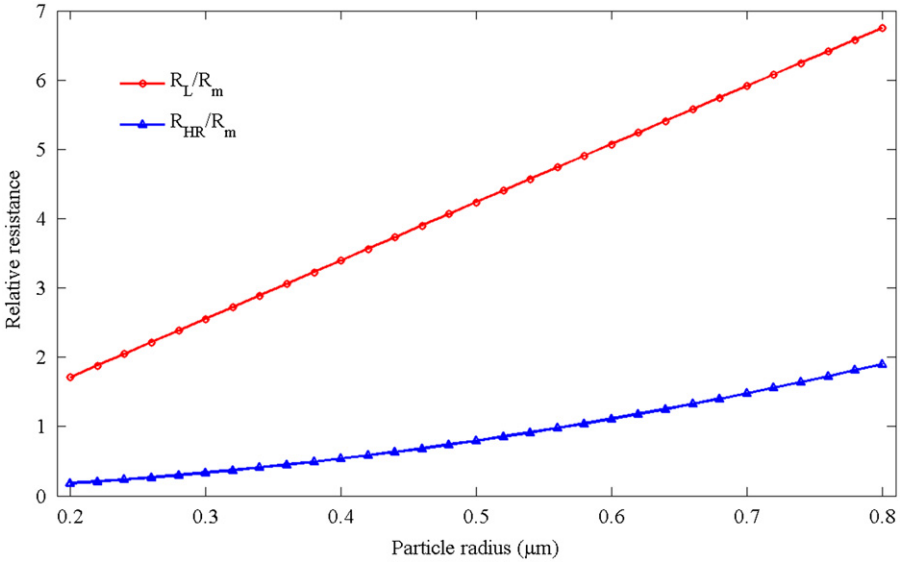

Fig. 6. Model results of R_L/R_m and R_{HR}/R_m for 30 μm-thick membrane with different particle radii, under $p_{H_2}=0.2$ atm and 973 K.

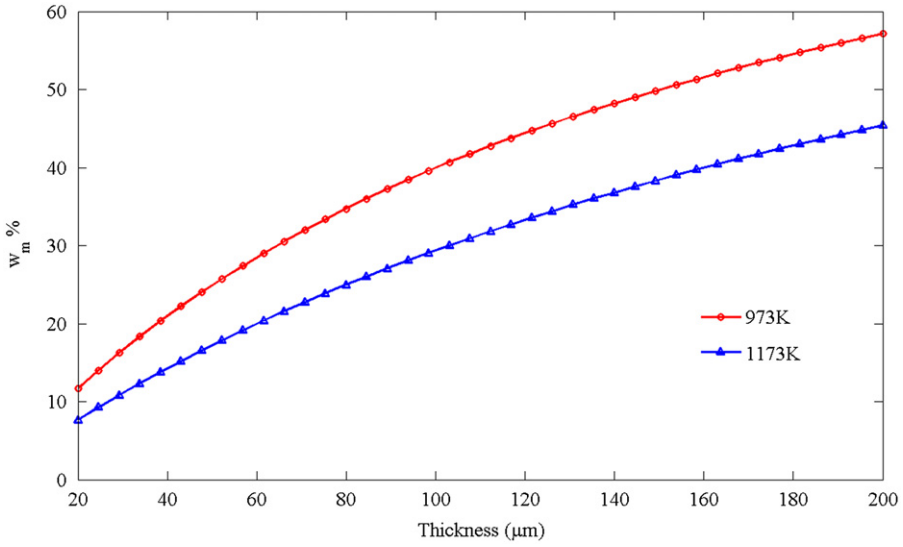

Fig. 7. Thickness dependence of w_m at 973 and 1173 K.

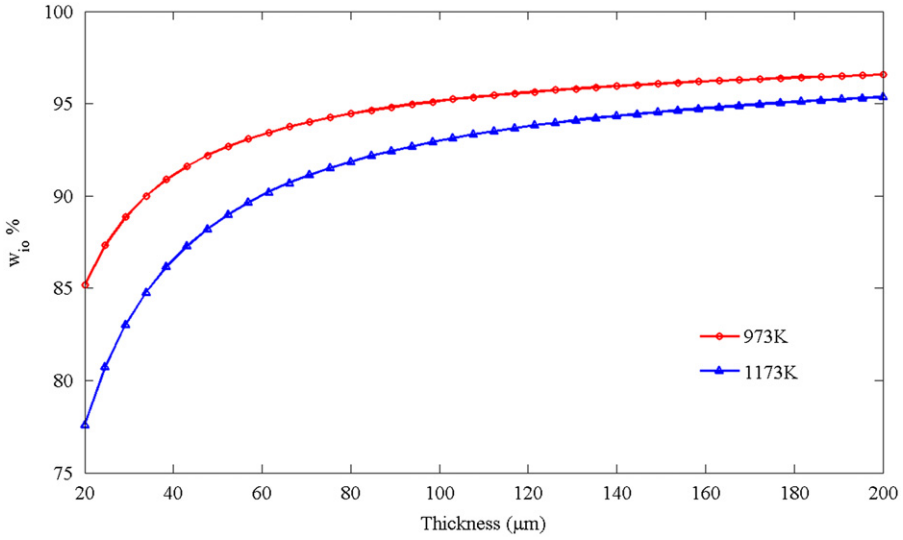

Fig. 8. Thickness dependence of w_{io} at 973 and 1173 K.

or surface modification at HL side is necessary to further enhance the permeation rate, because the reduction of membrane thickness has less effect for membrane already thinner than 40 μm. Besides, hydrogen permeation from Ni phase is remarkable for asymmetric membrane with thin dense layer. In summary, this model could be served as a guide to the fabrication and analysis of Ni–BZCY cermet asymmetric membrane.

Acknowledgments

This work is supported by Anhui Natural Science Foundation, and the Ministry of Science and Technology of China under Grant no. 2012CB215403.

Nomenclature

B	gas permeability constant in porous support (m^2)
C	OH_O^* concentration in BZCY phase (mol/m^3)
D_0	bulk diffusion coefficient of OH_O^* (m^2/s)
D_m	effective diffusion coefficient of OH_O^* for dense membrane (m^2/s)
D_s	effective diffusion coefficient of OH_O^* for porous support (m^2/s)
$D_{k,Kn}^{eff}$	effective Knudsen diffusion coefficient of gaseous species k (m^2/s)
D_{kl}^{eff}	effective binary diffusion coefficient of gaseous species k and l (m^2/s)
H	thickness of dense membrane (m)
J_{H_2}	total hydrogen permeation rate (mol m^{-2} s^{-1})
J_{io}	OH_O^* flux through BZCY phase (mol m^{-2} s^{-1})
J_{Ni}	hydrogen permeation through Ni phase (mol m^{-2} s^{-1})
K	equilibrium constant of step I in interfacial process (Pa^{-1})
k_1	forward rate constant of step II in interfacial process (mol m^{-2} s^{-1})
k_2	backward rate constant of step II in interfacial process (m/s)
L	thickness of the porous support (μm)
L_m	TPB length at dense membrane surface in unit area (m/m^2)

L_s	TPB length at porous support in unit volume (m/m^3)
p	hydrogen partial pressure (Pa)
P	percolation probability
F	flux of sweep gas (Ar) at HL side (mL/min)
R	equivalent resistance of related process (m^2 s $Pa^{0.5}$ mol^{-1})
r	particle radius (m)
r_g	pore radius (m)
S	effective cross section of the membrane (m^2)
T	temperature (K)
w	TPB width (m)
x_i	molar concentration of gaseous species i within substrate (mol/m^3)

Greek letters

θ	hydrogen atom coverage at Ni surface
δ	depth of the extended TPB area within support (m)
μ	Bruggeman factor
μ_m	dynamic viscosity of gas mixture (Pa s)
τ_g	tortuosity of the support
ϕ_g	porosity of the support
ϕ_{el}	volume fraction of Ni phase

Subscript

io	BZCY phase
el	Ni phase
MSI	membrane-support interface
L	hydrogen lean side

References

[1] K. Babita, S. Sridhar, K.V. Raghavan, Membrane reactors for fuel cell quality hydrogen through WGSR—review of their status, challenges and opportunities, Int. J. Hydrogen Energy 36 (2011) 6671–6688.

[2] H.F. Abbas, W.M.A. Daud, Hydrogen production by methane decomposition: a review, Int. J. Hydrogen Energy 35 (2010) 1160–1190.

[3] A.M. Amin, E. Croiset, W. Epling, Review of methane catalytic cracking for hydrogen production, Int. J. Hydrogen Energy 36 (2011) 2904–2935.

[4] H. Iwahara, T. Esaka, H. Uchida, N. Maeda, Proton conduction in sintered oxides and its application to steam electrolysis for hydrogen production, Solid State Ionics 3–4 (1981) 359–363.

[5] J.A. Labrincha, J.R. Frade, F.M.B. Marques, Protonic conduction in $La_2Zr_2O_7$-based pyrochlore materials, Solid State Ionics 99 (1997) 33–40.

[6] F. Krug, T. Schober, The high-temperature proton conductor $Ba_3(Ca_{1.18}Nb_{1.82})O_{9-\delta}$: thermogravimetry of the water uptake, Solid State Ionics 92 (1996) 297–302.

[7] S.W. Wang, F. Zhao, L.L. Zhang, K. Brinkman, F.L. Chen, Doping effects on complex perovskite $Ba_3Ca_{1.18}Nb_{1.82}O_{9-\delta}$ intermediate temperature proton conductor, J. Power Sources 196 (2011) 7917–7923.

[8] S.M. Fang, L. Bi, L.T. Yan, W.P. Sun, C.S. Chen, W. Liu, CO_2-resistant hydrogen permeation membranes based on doped ceria and nickel, J. Phys. Chem. C 114 (2010) 10986–10991.

[9] S. Erdal, L.E. Kalland, R. Hancke, J. Polfus, R. Haugsrud, T. Norby, A. Magrasó, Defect structure and its nomenclature for mixed conducting lanthanum tungstates $La_{28-x}W_{4+x}O_{54+3x/2}$, Int. J. Hydrogen Energy 37 (2012) 8051–8055.

[10] S.J. Song, E.D. Wachsman, J. Rhodes, S.E. Dorris, U. Balachandran, Hydrogen permeability of $SrCe_{1-x}M_xO_{3-\delta}$ ($x=0.05$,M=Eu,Sm), Solid State Ionics 167 (2004) 99–105.

[11] Y.M. Guo, Y. Lin, R. Ran, Z.P. Shao, Zirconium doping effect on the performance of proton-conducting $BaZr_yCe_{0.8-y}O_3$ ($0<y<0.3$) for fuel cell applications, J. Power Sources 193 (2009) 400–407.

[12] S. Ricote, N. Bonanos, A. Manerbino, W.G. Coors, Conductivity study of dense $BaCe_xZr_{0.9-x}Y_{0.1}O_{3-\delta}$ prepared by solid state reactive sintering at 1500 °C, Int. J. Hydrogen Energy 37 (2012) 7954–7961.

[13] W.P. Sun, Y.Z. Jiang, Y.F. Wang, S.M. Fang, Z.W. Zhu, W. Liu, A novel electronic current-blocked stable mixed ionic conductor for solid oxide fuel cells, J. Power Sources 196 (2011) 62–68.

[14] S. Tosti, Supported and laminated Pd-based metallic membranes, Int. J. Hydrogen Energy 28 (2003) 1445–1454.

[15] Z.W. Zhu, W.P. Sun, L.T. Yan, W.F. Liu, W. Liu, Synthesis and hydrogen permeation of Ni–$Ba(Zr_{0.1}Ce_{0.7}Y_{0.2})$ $O_{3-\delta}$ metal-ceramic asymmetric membranes, Int. J. Hydrogen Energy 36 (2011) 6337–6342.

[16] U. Beuscher, C.H. Gooding, The permeation of binary gas mixtures through support structures of composite membranes, J. Membr. Sci. 150 (1998) 57–73.

[17] U. Beuscher, C.H. Gooding, The infuence of the porous support layer of composite membranes on the separation of binary gas mixtures, J. Membr. Sci. 152 (1999) 99–116.

[18] A. Caravellaa, G. Barbieri, E. Drioli, Modeling and simulation of hydrogen permeation through supported Pd-alloy membranes with a multicomponent approach, Chem. Eng. Sci. 63 (2008) 2149–2160.

[19] X.F. Chang, C. Zhang, X.L. Dong, C. Yang, W.Q. Jin, N.P. Xu, Experimental and modeling study of oxygen permeation modes for asymmetric mixed-conducting membranes, J. Membr. Sci. 322 (2008) 429–435.

[20] Q.P. Zhang, T. Liu, Z.W. Zhu, L.Y. Hao, W. Liu, Modeling of hydrogen permeation for Ni-ceramic proton conductor composite membrane with symmetric structure, J. Membr. Sci. 415–416 (2012) 328–335.

[21] X. Wang, Kinetic monte carlo simulation of the elementary electrochemistry in a hydrogen powered solid oxide fuel cell, J. Power Sources 195 (2010) 4177–4184.

[22] P. Kerkhof, A modified Maxwell–Stefan model for transport through inert membranes: the binary friction model, Chem. Eng. J. 64 (1996) 319–343.

[23] Y. Vural, L. Ma, D.B. Ingham, M. Pourkashanian, Comparison of the multi-component mass transfer models for the prediction of the concentration overpotential for solid oxide fuel cell anodes, J. Power Sources 195 (2010) 4893–4904.

[24] H.Y. Zhu, R.J. Kee, A general mathematical model for analyzing the performance of fuel-cell membrane-electrode assemblies, J. Power Sources 117 (2003) 61–74.

[25] M. Ni, M.K.H. Leung, D.Y.C. Leung, Mathematical modeling of proton-conducting solid oxide fuel cells and comparison with oxygen-ion-conducting counterpart, Fuel Cells 4 (2007) 269.

[26] R.C. Reid, J.M. Prausnitz, T.K. Sherwood, The Properties of Gases and Liquids, McGraw-Hill, New York, 1977.

[27] M. Ni, D.Y.C. Leung, M.K.H. Leung, Electrochemical modeling and parametric study of methane fed solid oxide fuel cells, Energy Convers. Manage. 50 (2009) 268–278.

[28] B. Todd, J.B. Young, Thermodynamic and transport properties of gases for use in solid oxide fuel cell modelling, J. Power Sources 110 (2002) 186–200.

[29] J.H. Nam, D.H. Jeon, Comprehensive micro-scale model for transport and reaction in intermediate temperature solid oxide fuel cells, Electrochem. Acta 51 (2006) 3446–3460.

[30] S.B. Adle, J.A. Lane, B.C.H Steele, Electrode kinetics of porous mixed-conducting oxygen electrodes, J. Electrochem. Soc. 143 (1996) 3554–3564.

[31] Y.X. Zhang, C.R. Xia, A particle layer model for solid oxide full cell cathodes with different structures, J. Power Sources 195 (2010) 4206–4212.

[32] S.A. Steware, Review of hydrogen isotope permeability though materials, Lawrence Livermore National Laboratory, University of California, Livermore, California, ICR:53441.DE84 007362.

[33] Z.W. Zhu, Study of High Performance and Stability Ceramic Hydrogen Separation Membrane, Ph.D. Thesis, University of Science and Technology of China, 2013.